# LIGO - Treating Gravitational Events Lightly

P. Derek Bradshaw

University of Arizona – College of Optical Sciences

## Author Note

I would like to offer my gratitude to the California Institute of Technology, Massachusetts Institute of Technology, and the LIGO Scientific Collaboration for their public disclosure of LIGO's history and operations without which this paper would not have been possible. In addition, I would like to thank family, friends, and my review committee consisting of Professors Robert Norwood, Pierre Blanche, and Tom Milster of the University of Arizona for their contributions to improve the quality of this paper.

**Tables and Appendices are inserted in the back

---

Masters report submitted to the
**College of Optical Sciences**
In partial fulfillment of the requirements for the degree of
**Master of Science in Optical Sciences**
In the Graduate College of
**The University of Arizona**
**May 2016**

---

# Table of Contents

Abstract

The Light Interferometer Gravitational-Wave Observatory (LIGO) was devised in order to detect the magnitude and frequency of gravitational pulses from distant astronomical events. It does so through a complex system of noise correction, amplification of gravitational influence through Fabry-Perot cavities, and detection of fluctuations of light interference. This paper will analyze properties of the components comprising the LIGO interferometer, the methodology of facility operations and development stages, and then seek to statistically verify published attributes through Matlab simulation of the Fabry-Perot cavities. These cavities hold significant value to LIGO operations because photons carrying gravitational signals will spend the majority of their operational lives within these arms of the system.

The model will consist of three different functions: the first to handle photon interactions with cavity mirrors, returning the resultant reflection and transmission quantities. The second equation tracks the photon count within the cavity, and records specific positions of signal loss. Finally, the third is capable of summoning a histogram of overall trends in order to reach a conclusion of model behavior when compared to LIGO's published parameters

*Keywords*: LIGO, interferometer, Fabry-Perot, Matlab, photon

# LIGO - Treating Gravitational Events Lightly

Light is defined as a form of electromagnetic radiation perceivable to the human eye, and optics is a study of EM radiation ranging from infra-red to ultra-violet (visible spectrum inclusive). The study of light has evolved over centuries into the rather complex theorem of particle-wave duality, but the derivation of this topic alone has been the subject of thorough research and publication; therefore, I will forego its derivation while informing the reader that I will discuss applications of light waves to illustrate principles upon which LIGO functions, and use photonic or light particle analysis as means of statistical modelling at the end of this paper.

After Jean-Baptiste le Rond d'Alembert's solution of the 1D wave equation and Euler's subsequent 3D scalar wave solution, Maxwell's Equations were used in application with wave theory to yield the representation of light-wave propagation. This representation is mathematically written as a sinusoidal wave of the complex electrical field

$$\vec{U} = A * \cos\left(\vec{k} \cdot \vec{r} - \omega t + \phi\right) \tag{1a}$$

to be rewritten in the preferable Eulerian representation

$$\vec{U}(\vec{r}, t) = Ae^{i(\vec{k}\cdot\vec{r} - \omega t + \phi)} or\ \vec{U}(r, t) = \frac{A}{r} e^{i(kr - \omega t + \phi)} \tag{1b}$$

for plane waves and spherical waves respectively[1]. In these equations, the wavenumber $k = \frac{2\pi}{\lambda}$ and is given the direction of propagation when used as a vector, $r$ is the displacement (only scalar value needed for spherical representation due to radial symmetry), $\omega$ is the angular frequency of the wave, t is the referenced time after initial conditions, and $\phi$ is a phase change term included to allow the user more liberty with initial conditions (but can be removed altogether with skill in choosing initial conditions).

## Interference and Interferometry

In representing electromagnetic waves from light, optical engineers usually depict their analysis by use of ray tracing, an array of vectors denoting the directional propagation of radiation, or deformation of the wavefront, surfaces of identical phase that happen to lie orthogonal to ray trace vectors at every point of intersection. A simplified form of raytracing will be used in the diagrams to follow to show the ideal path of light through the system being analyzed. However, in the field of interferometry, most analysis bears a focus on the wavefront behavior of the light propagating through the system as a means of analyzing when two apparent light sources experience conditions of constructive and destructive interference [2].

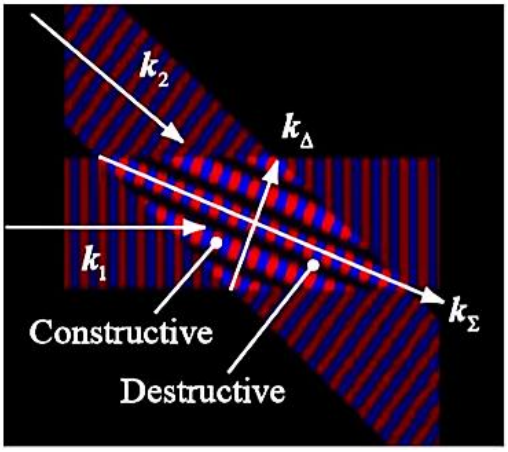


Figure 1- Two interfering plane waves [2]

The illustration to the left depicts a moment in time for two plane waves of different wavenumbers $\overrightarrow{k_1}, \overrightarrow{k_2}$ experiencing interference. The wavefronts are illustrated with red being surfaces of maximum positive field amplitude and blue being maximum negative amplitude of each individual wave. The rhombus of intersection shows interference, separated regions of constructive and destructive interactions along the vector, $\overrightarrow{k_\Delta} = \overrightarrow{k_1} - \overrightarrow{k_2}$. The regions of constructive interference or where the two waves are in phase (red on red, blue on blue) are therefore depicted in this illustration with more intense colors. The contrasting regions (shown as black) are out of phase; therefore, these are areas where the maximum positive of one field overlaps with the maximum negative of the other field (red overlapping with blue), yielding destructive interference or a location of zero net field value [2].

In real interferometry, this depiction needs to be expanded to include time variation of the interference pattern, including but not limited to losing the red and blue color scheme. However, the time-averaged result would still include bright and dark fringes to denote regions of constructive and destructive interference, which provide detailed information that can be used to analyze the

interaction between the two separate wavefronts. For example, fringe separation is found by $\Lambda = \frac{2\pi}{|\vec{k_\Delta}|}$, so a change in fringe spacing is a factor to determine changes in wavenumber separation, which can be related to spatial separation of the wavefronts (called optical path difference). One application of this particular principle was used by Albert Abraham Michelson in inventing the Michelson interferometer [3].

## Michelson Interferometer

In the case of a Michelson interferometer, the source beam is sent through a beam splitter of 50% reflectance and transmittance in order to divide the beam amplitude evenly between two paths. Each beam division (reflected and transmitted) is then sent along a radial arm towards a mirror that will retroreflect the beam back to the beam splitter. Upon return to the beam splitter, the transmitted beam and reflected beams are split once again in propagating toward the source and detector. The recombination causes the beams to create an interference pattern which becomes observable to

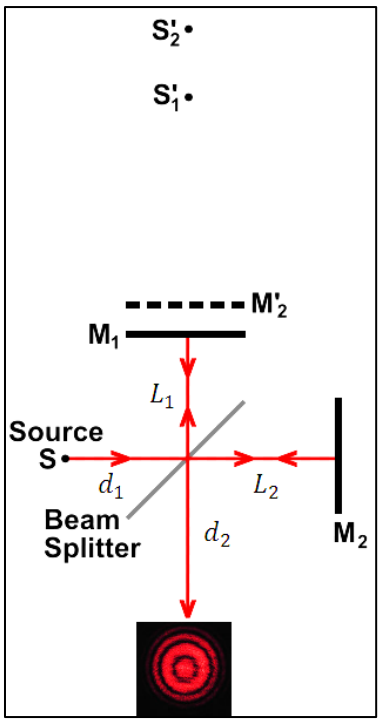


Figure 2 -Michelson interferometer setup and unfolded source positioning [3]

the detector. Accordingly, this interference pattern carries information of comparison between the arms based upon mirror alignment/tilt against the incident beams, as well as their optical path difference (OPD).

This process is more simply depicted by unfolding each beam's optical path length (OPL) about the test mirrors, $M_1$ and $M_2$ (as denoted in Figure 2). In this depiction, $M_2$ has a longer arm length, $L_2 > L_1$ which implies a longer OPL and therefore that its corresponding source image, $S_2'$ , would be further from image space than its counterpart $S_1'$ for the $M_1$ arm[3]. Since both beams travel the same length from the source to the beam splitter as well as from the beam splitter to the detector ($d_1, d_2$ respectively), the on-axis OPD can be written as

$$OPD = 2 * L_2 - 2 * L_1 = 2 * (L_2 - L_1) = 2 * \Delta L \quad (2)$$

due to the double-pass nature of the system along the arm lengths[2]. The OPD for a point $\varepsilon$ off-axis is solved by adjusting each OPL as the hypotenuse of on-axis and off-axis displacement.

$$OPL_1 = \sqrt{(d_1 + 2 * L_1 + d_2)^2 + \varepsilon^2} \quad (3)$$

In the event that two extended sources are oriented parallel in observation space, the resulting illumination creates circular fringes of equal inclination, otherwise called Haidinger's fringes. The fringe of maximum OPD rests at the

center, meaning that new fringes will emerge from the center as mirror separation increases [2]; conversely, a decrease in OPD will collapse rings and remove fringes from the center to the finite limit of equal OPL, or $OPD = 0$, where fringe visibility drops to zero due to the coinciding position of image sources (as depicted in the illustration below). It is important to note that fringe's linear separation and quantity recorded in a single plane (such as the detector's plane) depends upon OPD, while the phase separation is the same as previously discussed. Haidinger's fringes are important to the discussion of LIGO because they occur in Michelson interferometers as well as in Fabry-Perot systems, both of which are components of LIGO's design.

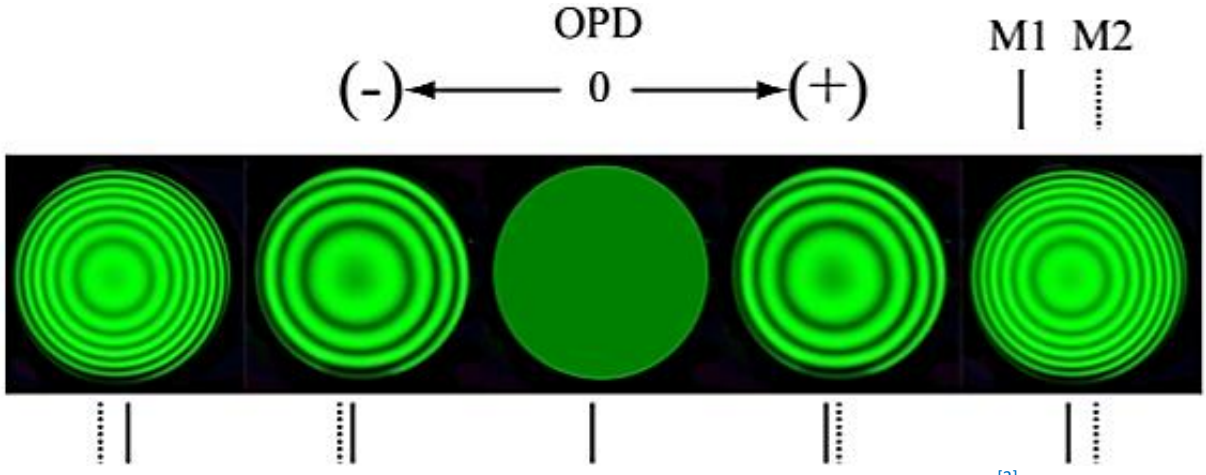


Figure 3 - Haidinger's fringes for two parallel mirrors for various OPD [2]

**Fabry-Perot**

A Fabry-Perot is defined as a cavity between two highly reflective surfaces. These surfaces could be the two surfaces of a glass, or two mirrored surfaces facing one another. Once light enters the cavity (through one of these surfaces), it will experience high probability of reflection and consequently, is contained for an extended duration of time while traversing the cavity length repeatedly. Fabry-Perot systems are useful in this attribute in that they increase the propagation distance of internal light waves. Figure 4 shows a general representation of a ray trace through a Fabry-Perot etalon. Internal confinement is depicted as well as each iterative ray of reflected and transmitted rays.

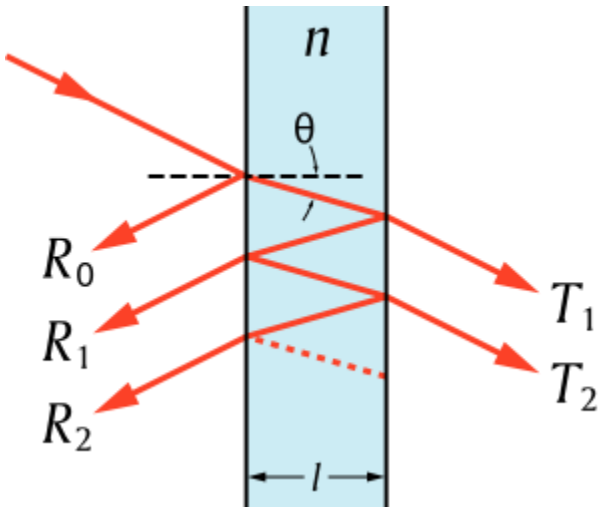


Figure 4 – Fabry-Perot etalon depicting internal reflections and exiting rays [4]

The phase difference between successive rays is determined by the spatial component of the illuminating wave (assumed to be planar) such that

$$\delta = k * OPD = \left(\frac{2\pi}{\lambda} * n\right) * (2 * l \cos\theta) \quad (4)$$

where the medium wavenumber $k$ is defined by the product of the wavenumber in free space and the cavity's index of refraction $n$. The optical path difference (OPD) is represented by the additional distance travelled within the media before recreating a plane wave with other escaping ray tracings [4].

Reflectance, Reflectivity, and Transmittance

The terminology used to identify a material may be confusing, but optical terminology is as important to understand as in any field of study. Reflectance is the intrinsic property for the glossy or shiny appearance of a material, and is commonly used to describe a thin object or film's ability to reflect an image. On the other hand, reflectivity of a material is the ability of a given substance to reflect as a thick sample, and is therefore the more accurate term in describing LIGO's thick components. In numerical quantity, reflectance is the ratio of reflected light to incident light while its converse, transmissivity defines the ratio of transmitted light to incident light for a given sample.

In calculating the reflectivity of a surface, the ratio of incident to reflected electrical fields is calculated (while other situations use ratios of Poynting vectors, radiance, spectral radiance, etc. are more correct in calculation and application).

The Fresnel coefficient $r$ is defined such that light travelling from medium 1 with refractive index $n_1$ to medium 2 with refractive index $n_2$ yields

$$r_s = \frac{n_1 \cos\theta_i - n_2 \cos\theta_t}{n_1 \cos\theta_i + n_2 \cos\theta_t} = \frac{\sqrt{\frac{\mu_2}{\varepsilon_2}}\cos\theta_i - \sqrt{\frac{\mu_1}{\varepsilon_1}}\cos\theta_t}{\sqrt{\frac{\mu_2}{\varepsilon_2}}\cos\theta_i + \sqrt{\frac{\mu_1}{\varepsilon_1}}\cos\theta_t} \tag{5a}$$

$$r_p = \frac{n_2 \cos\theta_i - n_1 \cos\theta_t}{n_1 \cos\theta_t + n_2 \cos\theta_i} \tag{5b}$$

for the subscripts $s, p$ representing the different polarizations of incident light possible [5], with $s$ being light polarized perpendicular to the plane of incidence and $p$ being light polarized parallel to the plane of incidence. Light in medium 1 with incident angle $\theta_i$ will cross the interface between media and emerge in media 2 with transmission angle $\theta_t$, which can be solved via Snell's law

$$n_1 \sin\theta_i = n_2 \sin\theta_t \tag{6}$$

However for normally incident light $\theta_i = \theta_t = 0$, the reflectance

$$R_s = |r_s|^2 = \left|\frac{n_1 - n_2}{n_1 + n_2}\right|^2 = \left|\frac{n_2 - n_1}{n_1 + n_2}\right|^2 = |r_p|^2 = R_p \tag{7}$$

Under normal incidence, the material reflectance $R$ is either the same value as $R_s$ and $R_p$, or is an average when both terms exist with the given illumination source: $R = \frac{R_s + R_p}{2}$.

The transmittance $T$ can either be calculated in a similar process using the Fresnel coefficient $t$ or can be calculated using conservation of energy s.t $T = 1 - R$, with no material absorption or scattering assumed [5].

Finesse

In order to accurately observe the peak resolution of the transmitted wave signal, it is important to have a measure potential overlap that occurs between the 2 waves. For a Fabry-Perot cavity, reflectance can be used to define the coefficient of finesse $F = \frac{4R}{(1-R)^2}$, which is related to the finesse itself by

$$\mathcal{F} = \frac{\pi}{2 * \arcsin\left(\frac{1}{\sqrt{F}}\right)} \cong \frac{\pi\sqrt{F}}{2} = \frac{\pi\sqrt{R}}{1-R} \tag{8}$$

for which the approximation is accurate for R close to 1 [4]. When mirror reflectance differs on each side, the finesse is expressed in terms of an effective reflectance

$$R = \sqrt{R_1 R_2} \tag{9}$$

Finesse is experimentally defined as the free spectral range (FSR) divided by the linewidth (width of the pulse when measured at the middle of its amplitude or the “full width half maximum” value). Therefore, a smaller width denotes a larger ratio of frequency separation to width and therefore a more resolvable signal.

**Creation and use of LIGO.** As Albert Einstein published his formulas of field theory and thereby finalized his theory of relativity (an event now celebrating its centennial), he shared his prediction that the gravity itself was a field propagating as a wave in space-time that travels at the speed of light. In the years, following, this prediction evolved as theoretical scientists created solutions for astronomical bodies and interactions between celestial bodies. In recent years, momentum on this field of study grew and these solutions were applied towards modelling multi-body interactions and formulating theoretical waveforms, thereby creating a focus of specifications of bandwidth and amplitude sensitivity needed to record or measure a real-time event.

Simultaneous to the modelling phase of theory, other scientists and engineers were tackling the effort of system detector design. At first, designs were focused towards analysis of matter resonance under the influence of gravitational waves. However, when replicating results proved difficult, the community gravitated towards detection via interferometry (please forgive the pun). The focus of an international eye on the field of interferometry became a blessing to the field, as studies were placed on the limitations of the system due to noise and tests of performance. This process resumed into the turn of the millennium, when an international network of detectors was funded into

construction and operation: TAMA 300 in Japan, GEO 600 in Germany, Virgo in Italy, and the Laser Interferometer Gravitational-Wave Observatory (LIGO) constructed at two locations in the United States [6].

The LIGO proposal was written by Rochus E Vogt et al (a group of investigators hailing from Cal Tech and MIT) and submitted to the National Science Foundation in December 1989. This document was clear in outlining that LIGO's design would focus on two components: the detection of gravitational waves, as well as gauging design performance towards advancing detector development as a whole. Therefore, the original proposal included 3 phases of construction, which incorporated foresight of confirmed measurements in conjunction with future revision as discovery and scientific needs of gravitational-wave astronomy as a field evolved. I would highly recommend consulting the document itself for additional details [7].

*Phase A*:

Site 1 is equipped with 2 Fabry-Perot cavities within a vacuum, one of full length while the second is placed with only half the interferometric arm length. This is designed so that the half-length cavity can experiment with test masses, beam splitters, etc. and components may be exchanged without depressurizing the cavity arm. Meanwhile, the full length cavity of Site 1 can work in conjunction with the full length cavity of Site 2 towards actual observation of gravitational waves, while the half-length Fabry-Perot may add additional information for operating frequencies when placed in observation mode. The three interferometer system constitutes a "triple-coincidence" detector (basically meaning if a signal shows up on multiple detectors, it is not anomalous) and is the principle technique for establishing conclusive results. This phase of construction is capable of analyzing

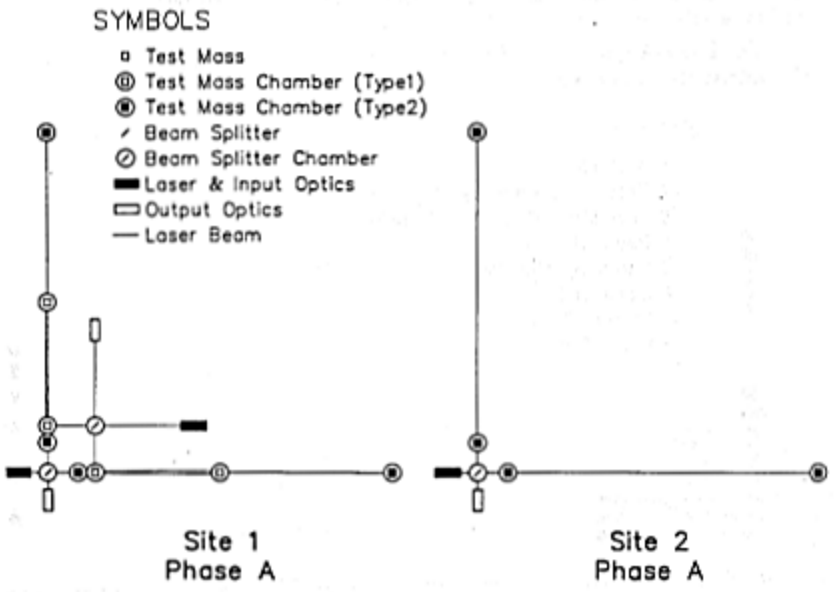


Figure 5a– Initial development design (Phase A) [7]

detector efficiency (via the half-length cavity) while not interrupting the detection efforts of the full length Fabry-Perots.

*Phase B*:

Doubling the components of Phase A, Phase B grants site 1 two full length and two half-length cavities and adds a second full length Fabry-Perot to site 2. Doubling the number of operational detectors and expanding the system so than any of the components may be replaced without de-pressurizing the cavity allows indefinite observation from at least 1 detector while the other is under maintenance or update. Furthermore, when both triple coincidence detectors are designed to be mutually exclusive of signal (traversing the same cavity in parallel with no significant scattering), the system is capable of making two independent

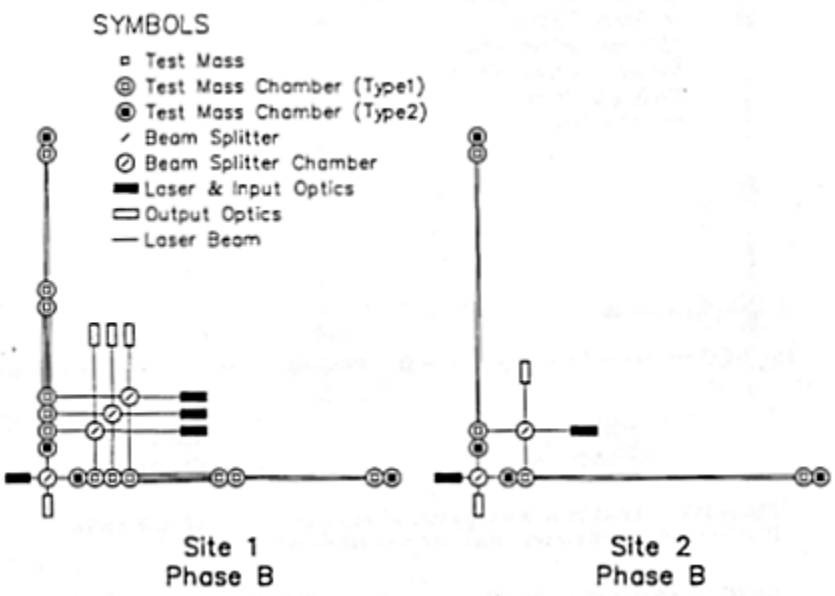


Figure 5b – Phase B of development [7]

observations of the same event(s) concurrently. The conclusion is that this phase denotes the operational efficiency limit of interferometric design for the facility.

*Phase C*:

This diagram may appear a minor modification, but phase C is simply a third detector port added to the system. However, this 3rd leg of construction was added to the design to provide for "special investigations" and open access to the scientific community. As an international effort to detect gravitational waves, I would venture to say that this addition to the interferometer would share details of design with academic peers as well as educate guests without hindering the efforts of the project as a whole.

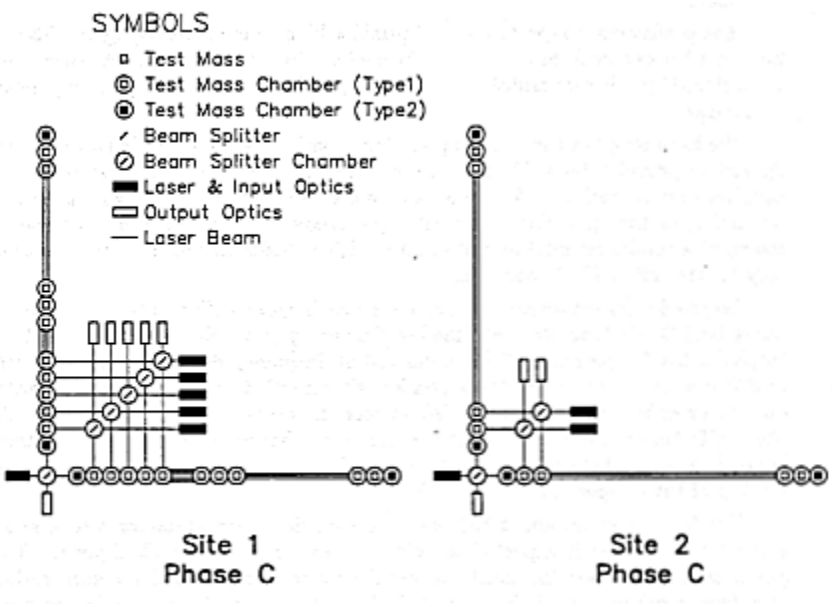


Figure 5c – Tentative design for Phase C [7]

Also to relate his foresight on the design, Vogt wrote "Phase C, as currently envisaged, is our present best concept for the evolution of the LIGO. In practice,

the discoveries in Phases A and B will guide further development." (Vogt 39). Generally speaking, Vogt presented a detailed plan to the NSF to show that LIGO and its operators have vision for subsequent growth of the gravitational wave detection community, but also formally stated that the design and advancement of LIGO would shift if detector analyses from early stages of LIGO, or gravitational theory, deem it to be necessary. Accordingly, LIGO's emphasis on adaptive components and open port design cater extremely well towards the unforeseen developments [7] (page 36-39).

Figure 6 – Initial LIGO design as presented in the NSF proposal [7] (page 44)

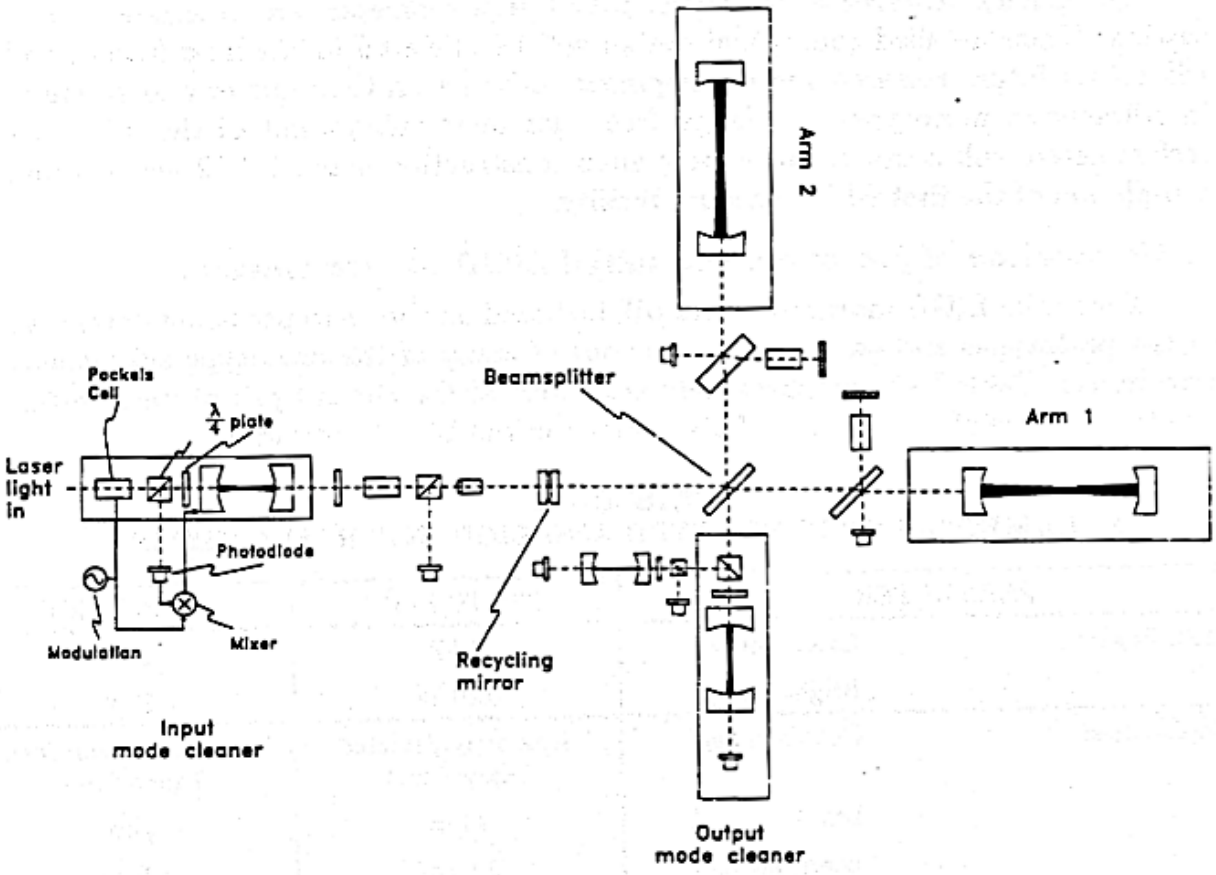


LIGO functions as a variant of the Michelson interferometer design, with Fabry-Perot cavities contained within the arms of the interferometer. Unlike a normal Michelson that experiences the linear phase change described in equation 4, the addition of a front cavity mirror to the arm mirror (with reflectances $R_1$ and $R_2$ respectively) causes a nonlinear phase transition from $-\pi$ to $\pi$. As $R_1$ changes from 0 towards 1, the phase transition grows more intense, approaching a step function about $OPD = 0$ [2]. LIGO implements this feature with many additional components to help control further engineering results towards the desired aim.

For the initial LIGO design, key features were the mode cleaner for the input laser, beam splitter analysis, Fabry-Perot arms, recycling mirror, and the mode cleaner at the output port preceding final results.

Input mode cleaner- A mode cleaner is used to correct the laser light illuminating the interferometer arms for a constant frequency. This mode cleaner is a small Fabry-Perot cavity whose resonance is measured by the laser modulated via radio frequency from the Pockels cell. Once the cavity length is measured, a corrective signal is returned to the laser as feedback, locking the laser source into the specific frequency. Another system is placed behind the cavity to insure that the phase entering the interferometer arms is of matching resonance [7].

Fabry-Perot cavities- As light transfers into the Fabry-Perot arm cavities, it will propagate forward and backward repeatedly due to the high reflectivity of the cavity mirrors. In LIGO, it is important that the cavity be calibrated such that incident light will resonate with light already contained with the cavity, thereby increasing the intensity of beam within the cavity. In general, higher intensity will contribute greater ability to detect gravitational waves while simultaneously contributing greater noise to the system, in the forms of thermal expansion and radiation pressure upon the test masses [7].

When a gravitational wave propagates through LIGO, it will continue unhindered through the system but alter the space orthogonal to the vector it travels. When this occurs across the LIGO system, one cavity arm will expand while the other arm (lying orthogonal) experiences contraction, and then alternate to the original arm shrinking while the secondary expands. Both of these changes occur on such a minuscule scale that detection is excruciatingly difficult, but are of interest because the magnitude of distortion is proportional to gravitational wave amplitude while the rate of alternation can be related to the wave's frequency [7].

At the same time gravity alters the cavity length, the photons propagate the new cavity length and experience a phase change as one cavity's photons travel the added distance and the other cavity experiences opposite phase change due to cavity curtailing. This effect is much more applicable due to the nonlinear phase change from the Fabry-Perot cavity. To illustrate, photons experience the first phase change, rebounding off the end test mass (ETM) and traveling the new length to the initial test mass (ITM) where some photons will be transmitted to relay the cavity change to the detector. On the other hand, the reflected light will repeat the process of cavity reflection, incurring further altering of phase due to the photon's propagation speed relative to the cavity's recovery rate from

gravitational influence. The nonlinear phase changes due to Fabry-Perot multi-passing amplify the observed effect of gravitational waves upon light phase (predicted to magnify the effects of gravitational waves by a factor of 300 [6]) .

Beam splitter feedback- A high transition plate (~99%) is placed at 45° between the beam splitter and interferometer arms in order to make corrective adjustments and gather preliminary data. The beam arriving from the beam splitter is minutely deviated to measure beam alignment within the cavity, and the beam splitter's position is corrected accordingly. In addition, the signal exiting the Fabry-Perot cavity is measured for cavity resonance (test masses are adjusted into a stable resonance condition for cavity saturation). Secondly, this measurement also doubles as a preliminary measure of gravitational wave output on for a single anti-symmetric arm [7].

Recycling mirror- A highly reflective mirror (transmission of a couple percent) is placed before the beam splitter such that the portion of beam exiting the cavity that would return in the direction of the laser source is retro-reflected back into the cavity arms. This serves to create a cavity feeding into the Fabry-Perot arm cavities, further increasing the power or beam intensity within the arms themselves [7].

Output mode cleaner- This mode cleaner is placed before the detecting photodiode in order to mitigate the effects of scattered light within the system [7].

*Advanced LIGO (aLIGO)*. After the initial LIGO's system limitations were analyzed and their sources correctly identified through a rigorous process of mathematical modelling and statistical analysis of output data to noise, each and every component of LIGO was revised (in many cases redesigned altogether) and additional components were created. By more accurately restricting the sources of noise, aLIGO is better calibrated for accurate detection of gravitational waves, as well as equipped for a larger cosmic range of detection (as the restriction of noise factors allows the system to more visibly observe gravitational waves that would have otherwise dissipated below the system sensitivity)

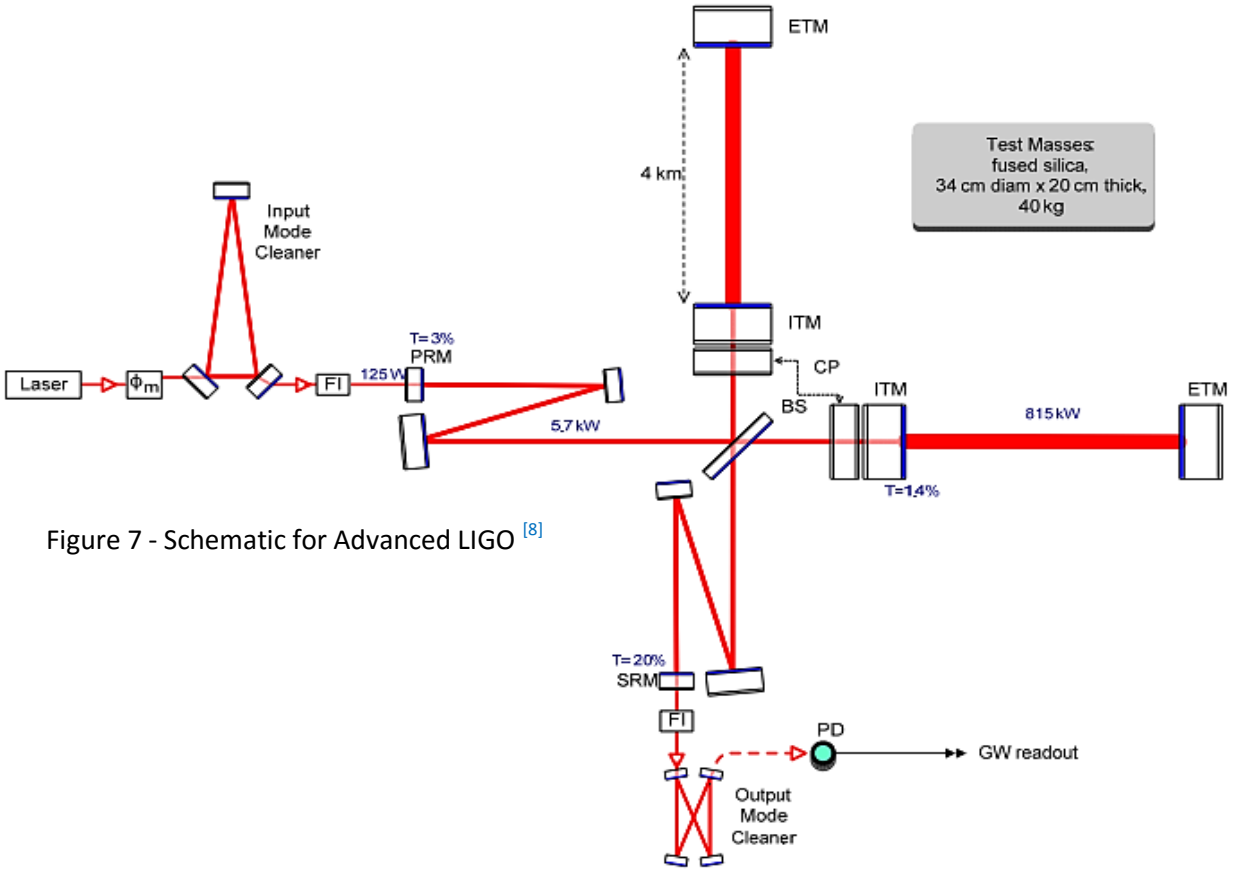


Figure 7 - Schematic for Advanced LIGO [8]

Laser- The Nd:YAG laser is increased from 10 W to approximately 180W output in order to improve the "quantum-limited" sensitivity of photon behavior. Starting with this change focuses on strengthening all signals, while demanding a greater control of noise by the remaining system components. However, this laser beam still travels through a ring cavity for "mode cleaning" and a reflective mode-matching telescope (same as in initial LIGO).

In addition, the laser light is sent through focusing reflective telescoping, allowing the beam to condense to a smaller spot size. This is useful not only in

decreasing the needed size of the preliminary mirrors, but brought the added effect of enabling the recycling mirrors' cavity to stabilize on the fundamental optical mode ($TEM_{00}$) [8].

Test Masses – Initially test masses were 25cm diameter, 10cm thickness at 11kg but have been increased to 34cm diameter, 20cm thickness measuring in at 40 kg. The reasoning behind this change is two-fold, and is highly dependent upon the nature of photons. In quantum mechanics, a photon is attributed to possessing momentum and energy, and both of these become problematic during their interaction with test masses in the arms of the interferometer.

As photon momentum is transferred to the test masses, they experience small but noticeable recoil due to the principle of radiation pressure. This recoil may be too small for the human eye, but for LIGO's measurements based upon the separation between the test mass surfaces to the highest precision possible, it became a factor observed in the initial LIGO design. Notwithstanding, by increasing the mass of the test surfaces, they became more resistant to the effects of radiant pressure. To clarify, the increased mass grants the mirrors a higher inertia value which by the conservation of momentum in classical physics, results with a smaller displacement under a given collision.

Similarly, photon energy is a contribution to thermal expansion. When photons interact with matter (in this case the test mass surfaces), some photons are absorbed by atoms within the test mass and the transfer of energy becomes manifest by molecular excitation and thermal energy. On a larger scale, these excitations increase separation between atoms and therefore expand the size of the material and is therefore called thermal expansion. This expansion is a problem for LIGO not only because the thermal expansion at both mirrors decreases the cavity length, but also because the thermal expansion at the specific region where the laser reacts with the test masses causes a localized change in mirror curvature (potentially creating unintended scattering).

However, increasing the mirror size also limits the effects of thermal noise. First, a larger test mass is able to disperse thermal energy better (distributing the overall thermal expansion more evenly). Secondly, the region of mirror surface experiencing localized heating will be more stable. This is because the larger diameter, the mirror curvature is not as high and therefore a small deformation of radius is not as noticeable as for a mirror with high curvature [9].

Figure 8 – Quadruple Pendulum Design [9]

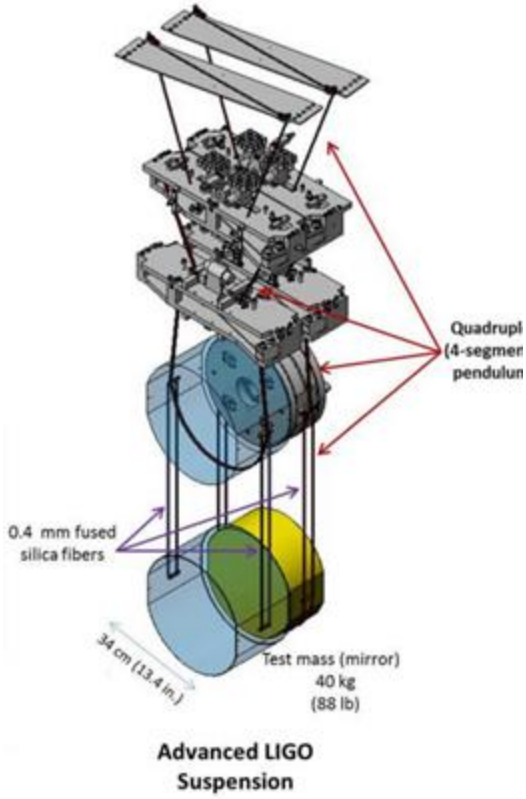


Quadruple pendulum silica fiber- In order to improve the seismic isolation of system components, each LIGO component was hung as a pendulum with steel cables on a seismically dampening platform. However, aLIGO reduces seismic noise further by hanging each valuable component by an intricate system of quadruple pendulums as pictured in figure 8. Each pendulum dampens the oscillation motion of the pendulum preceding it, restricting the effects of earth's motion even further. In addition, the steel cables were exchanged for a set of 0.4 mm fused silica fibers that still contain sufficient tensile strength, but are not subject to the same vibrational resonance as steel (possessing an amorphous as opposed to polycrystalline molecular structure) [9].

Signal recycling mirror- In order to preserve the effects of gravitational shift, a signal recycling mirror (10% transmissivity) is placed at the exit of the interferometer so that gravitational wave "sidebands" created are capable of being retro-reflected into the system. The designs for aLIGO state that the storage

or extraction of this signal from the system is dependent upon the signal recycling cavity's resonance, therefore opening the system to the possibility of cavity tuning towards the source.

Though the creation of another recycling mirror system creates more degrees of freedom in the system that must be monitored (particularly mirror angles and cavity mode resonance), aLIGO became able to use these added degrees of freedom to analyze system restrictions and response. During broadband tuning, staff members were able to observe compartmentalized sources of quantum noise strength towards low and high frequency analysis, and thermal noise of test mass coatings towards the mid-range. In addition, broadband tuning manipulated the ratio of mirror excitation due to radiation pressure and yielded an increase of resolution [8] (page 6).

The final effect observed with the signal recycling cavity was power control at the beam splitter. The beam splitter began to experience thermal distortion due to the higher intensity beams, thereby creating a functional issue, especially with the elliptical pattern of illumination on its surfaces. However, the signal recycling cavity created an interferometric response that facilitated lower power at peak sensitivity [8] (page 36).

Output mode cleaner- Another mode cleaner is placed before the detecting photodiode in order to isolate the desired signal. The system is designed for a filtered analysis of $TEM_{00}$, though other modes will still exist within the output beam. The purpose behind the output mode cleaner is to substantially reduce the observed power of these signals (as well as an RF source signal near the output port) below the desired noise threshold, as well as to mitigate the effects of scattered light proceeding through the system [8].

Active correction of thermal lensing- Continued efforts have been placed to reduce and correct the effects of thermal lensing, the effect of thermal expansion on a lens as well as some materials with thermally sensitive indices. Some forms of correction have already been mentioned: the increased size of test masses, as well as the signal recycling mirror's control of peak power incident on the beam splitter. In like manner, LIGO is researching other possible solutions of mitigating thermal effects, such as lens shaping accounting for expected surface distortion, less thermally-sensitive lens coatings, or introducing negative lensing materials (having $\frac{dn}{dt} < 0$) for optical result corrections [8].

*System Modelling*. In mathematically modelling LIGO, I will focus on modelling the behavior of light within the Fabry-Perot arm cavities, therefore considering the portion of the system under the most gravitational warping. This model will consist of two portions: the first considering the lifetime of a singular photon packet sent into the cavity, while the latter model will consider a single packet that will experience additional photon injection upon each correspondence with the initial test mass (ITM). This analysis is an oversimplification of LIGO's operations in that the photon injection term $I$ will be treated as a constant rather than a random variable, as well as the miniscule Raleigh scattering within the cavity and test mass absorption terms are ignored. The single packet analysis could be expanded to analysis of a single pulse of modal behavior, but since LIGO holds strong focus upon the fundamental cavity mode, this representation is better described as a spatially isolated region allowed to propagate within the cavity.

Part I: Single Packet Injection

The single packet injection will be used in order to analyze expected photon lifetime within the cavity, as well as the decay rate corresponding to the single pulse entry. In using the information from Table 1 (included before the appendix

section), it is possible to calculate the statistical outcome of ETM and ITM interactions. For mirror transmissions $T_{ITM} = 1.4\% = .014$ and $T_{ETM} = 10ppm = .00001$, the complementary reflectivities are $R_{ITM} = 1 - T_{ITM} = .986$ and $R_{ETM} = .99999$. These variables in conjunction with the independence of reflection probability for the two mirrors permit the expected duration of cavity confinement of $I$ photons to be written as

$$\mathrm{E}[n] = \frac{I}{2} = I * P(reflection\ at\ ITM)^{n} * P(reflection\ at\ ETM)^{n,n+1} \quad (10)$$

for $n$ cavity cycles (the ETM probability is written with $n, n+1$ because this mirror will have either the same or one more interaction than ITM for any given photon) and $P(\dots)$ representing the probability of the statement enclosed. Dividing $I$ from both sides of the equation generalizes the result to a single photon

$$\frac{1}{2} = P(reflection\ at\ ITM)^{n} * P(reflection\ at\ ETM)^{n,n+1} \quad (11)$$

For a mirror interaction, the probability of reflection can be written as the reflectivity of that surface (previously defined as a ratio of beam intensity, which is just a larger scale probability). Generalizing the situation so that each reflection occurs $n$ times

$$\frac{1}{2} = (R_{ITM}R_{ETM})^{n} = (.986 * .99999)^{n} \Rightarrow n = 49.1283 \quad (12)$$

Using this to analyze the 49th through 50th cycle:

The 49th cycle would be $(.986 * .99999)^{49} = .500906$

The additional reflection off of ETM gives $(.986^{49} *. 99999^{50}) = .500901$

which is still too small. Finally, at the 50th full cycle $(.986 * .99999)^{50} = .493888$ finally crosses the half-life condition of cavity duration such that $n_{50\%} = 50$.

Using the same process to find the expected number of cavity cycles for 1% photons and 0.1% photon residual, the process yields $n_{1\%} = 327, n_{0.1\%} = 490$ cycles respectively.

The code itself will focus on 3 different functions: determining the number of photons reflected upon mirror contact, recording photon population with the number of photons lost (via use of the published transmission value) at each cycle, and then a histogram analysis using marked checkpoints from the population analyses of several independent packets. Using Table 1, the transmission values $T_{ITM} = 1.4\%$, $T_{ETM} = 10ppm$ yield the optimistic reflectance values $R = 1 - T \Longrightarrow R_{ITM} = .986$, $R_{ETM} = .99999$. Then simply generating a random uniform percentage for each photon upon mirror interaction, and allowing values greater than the mirror's reflectance to exit the system is enough to create a stochastic variable of photon transmission.

Appendices A-C include graphs of population decline, photon transmissions per cycle (for ITM isolated and total of ITM+ETM together per cycle), and variable information for $I, n_{50\%}, n_{1\%}$, and $n_{0.1\%}$**. The most noticeable trend is that as photon packet size $I$ increases, the randomness of transmissions becomes less visible due to larger overall values compared to the fluctuations from trending behavior. Furthermore, this finding is also supported in Tables 3, which shows a general decrease in sample standard deviation as photon count $I$ is increased. I would also like to point out that Tables 2 and 3 together show that changes in $N$ (number of independent trials) or $I$ do not increase precision on determining the various decay positions ($n$), but that sampling always gathers around the proper vicinity.

In addition, the following histograms of $n_{50\%}, n_{1\%}$, and $n_{0.1\%}$ show the statistical trend of $I = 100{,}000$ photons for increasing $N$. These histograms were generated by taking $N$ identical but independent plots similar to those in Appendices A-C, and then using the recorded cavity cycle positions $n$ for 50%, 1%, and 0.1% (each depicted in said appendices). These independent trials served as a statistical sampling that is then used to analyze trend behavior for the cavity itself. Though histogram appearances show a structural variance, the normalized curves progressively take shape.

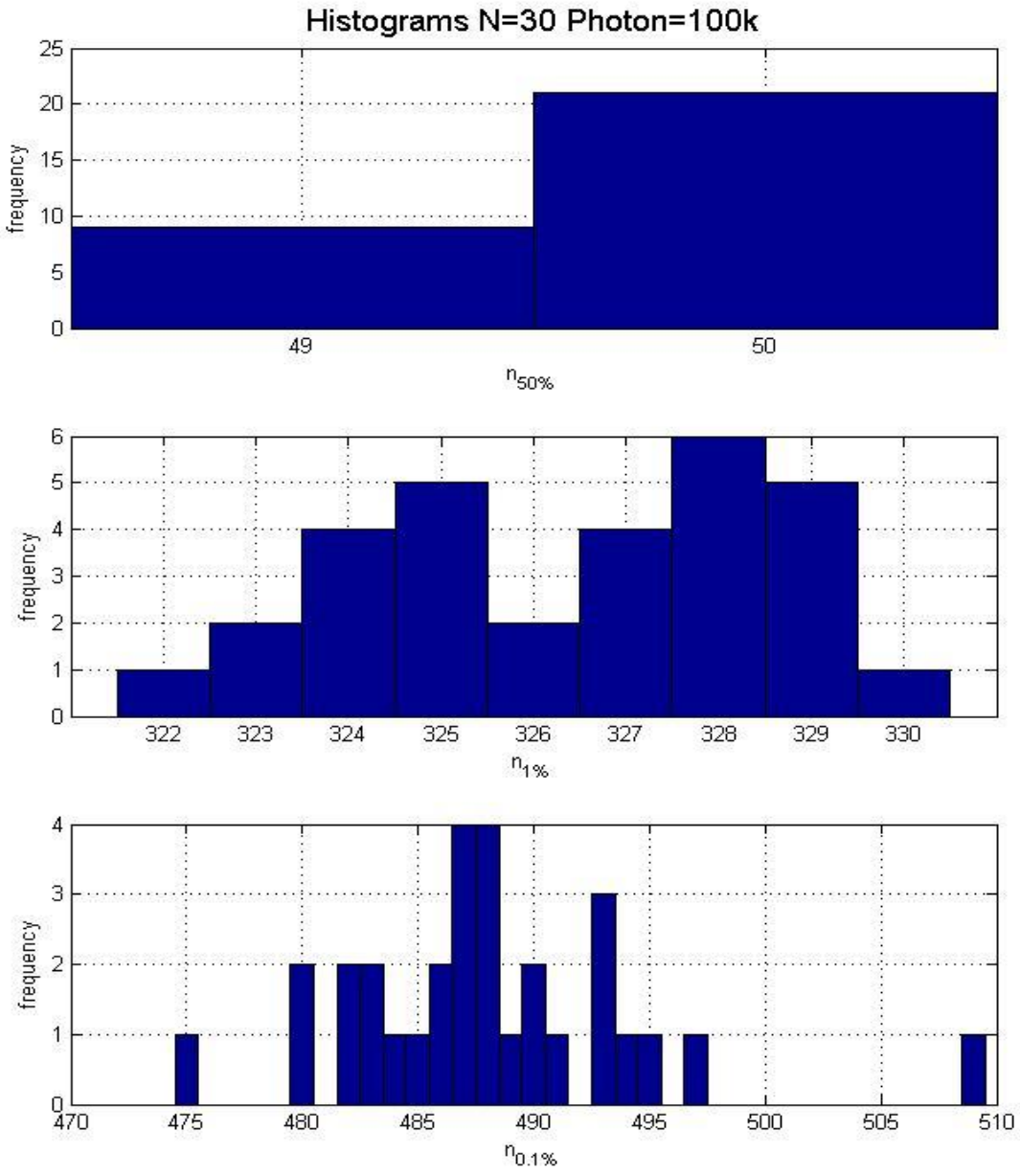


Figure 9a – Histograms of $n_{50\%}, n_{1\%}$, and $n_{0.1\%}$ for $N = 30, I = 100k$

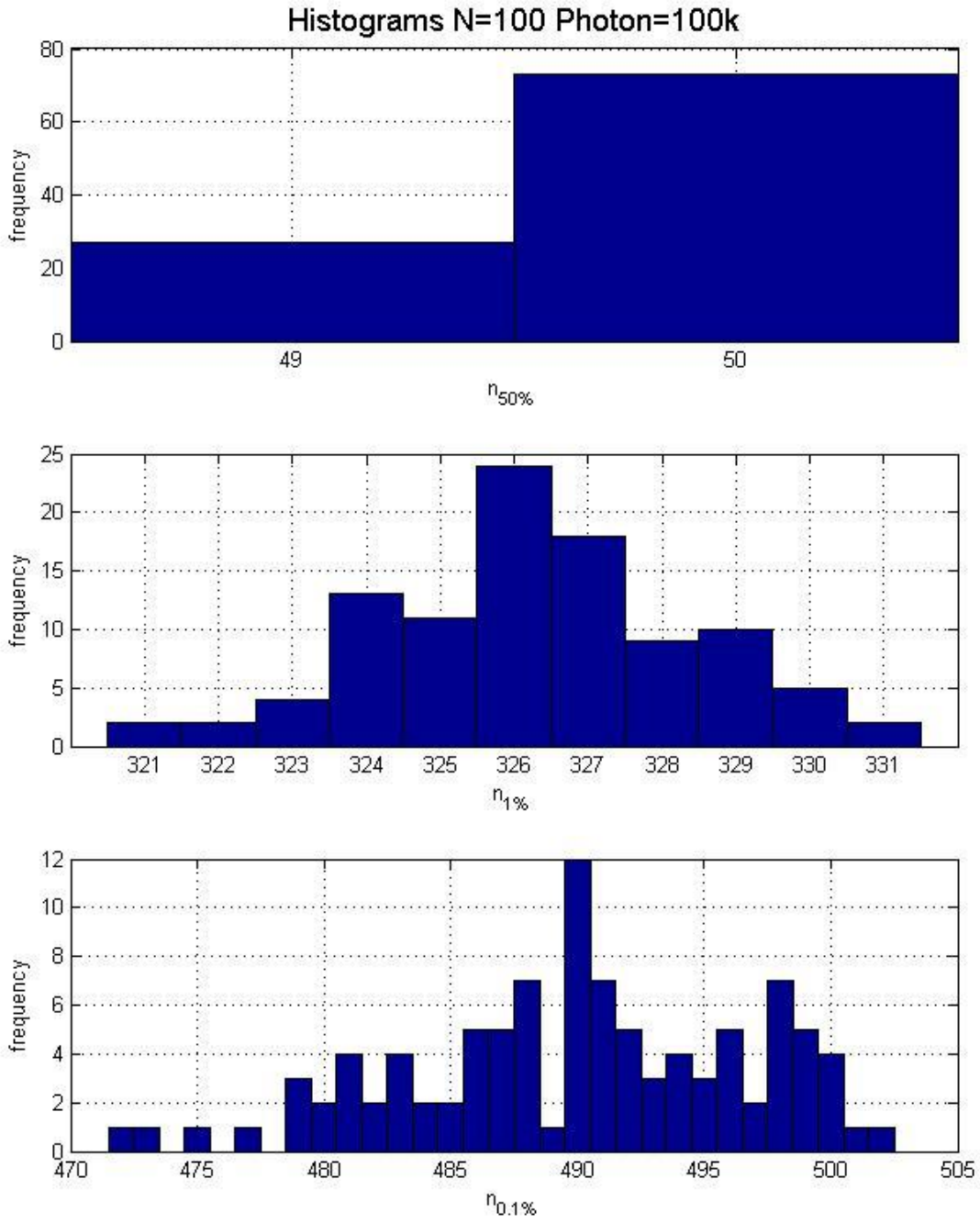


Figure 9b – Histograms of $n_{50\%}$, $n_{1\%}$, and $n_{0.1\%}$ for $N = 100$, $I = 100k$

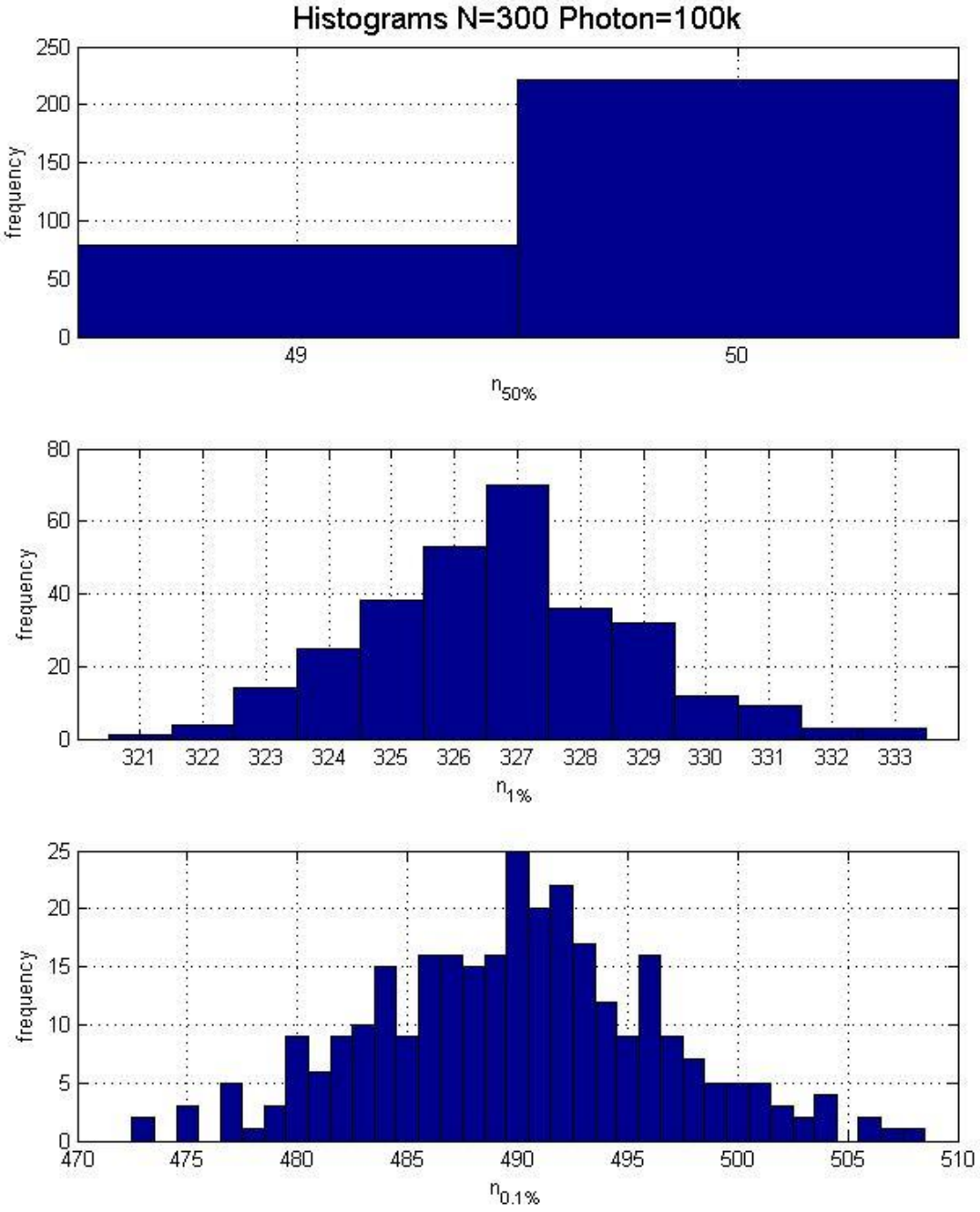


Figure 9c – Histograms of $n_{50\%}, n_{1\%}$, and $n_{0.1\%}$ for $N = 300, I = 100k$

As each histogram gathers around the expected number of cycles, the conversion into expected propagation distance and time are a small calculation

$$d_{50\%} = 8km * n_{50\%} = 8km * 50 = 400km \quad (13)$$

$$\Rightarrow t_{50\%} = \frac{d_{50\%}}{c} = 1.333ms \quad (14)$$

$$d_{1\%} = 8km * n_{1\%} = 8km * 327 = 2616km \Rightarrow t_{50\%} = \frac{d_{50\%}}{c} = 8.72ms$$

$$d_{0.1\%} = 8km * n_{0.1\%} = 8km * 490 = 3920km \Rightarrow t_{50\%} = \frac{d_{50\%}}{c} = 13.067ms$$

This expected value of $t_{50\%}$ differs slightly from the 1.7ms given in table 1, but is on the same order for my simplified analysis.

Part 2: Cavity Saturation

The second portion of my math model seeks to test the Fabry-Perot for saturation behavior. In similar fashion, this portion is subject to many oversimplifications that serve to mitigate the computational burden that this model demands by nature. Nevertheless, this model utilizes a photon packet injection upon every complete cycle, such that cavity population (representative of cavity beam intensity) builds over time. Using the same photon injection term $I$, as well as mirror reflectances $R_1$ and $R_2$, the total cavity population after $n$ cycles equals

$$S_n = \left([I * (R_1R_2) + I] * (R_1R_2)\right) + \cdots \tag{15a}$$

Distributing each of the $(R_1R_2)$ reflections inside each grouping allows this summation to be rewritten as

$$S_n = \sum_{k=0}^{n} I * (R_1R_2)^k = \sum_{k=0}^{n} a_k \tag{15b}$$

where $a_k$ is a representation of a cavity confined photon packet after k cycles. To find the final saturation population value as a factor of the injection term

$$S_n = A * I = I * \sum_{k=0}^{n} (R_1R_2)^k \tag{16}$$

Since the latter term is a geometric series

$$A = \frac{1}{1 - R_1R_2} = 71.3783 \tag{17}$$

meaning that the cavity saturation point should be $\approx 71.38$ times the value $I_{in}$.

However, true saturation occurs when $I_{out} = I_{in}$, so it is more vital to track the $I_{out}$ variable, which can be written as

$$I_{out} = \sum_{k=0}^{n-1} I * (1 - R_1R_2) * (R_1R_2)^k \tag{18}$$

or the summation of photons that are successfully contained for k previous cycles, just to be removed on the final cycle. This interpretation is attractive because

these individual packet values are already represented by the second plot in Appendices A-C, meaning that an integration of the transmission plot (like pictured below in Figure 10) up to the cavity loop value of $n$ can quickly calculate the value of $I_{out}$ after $n$ cycles.

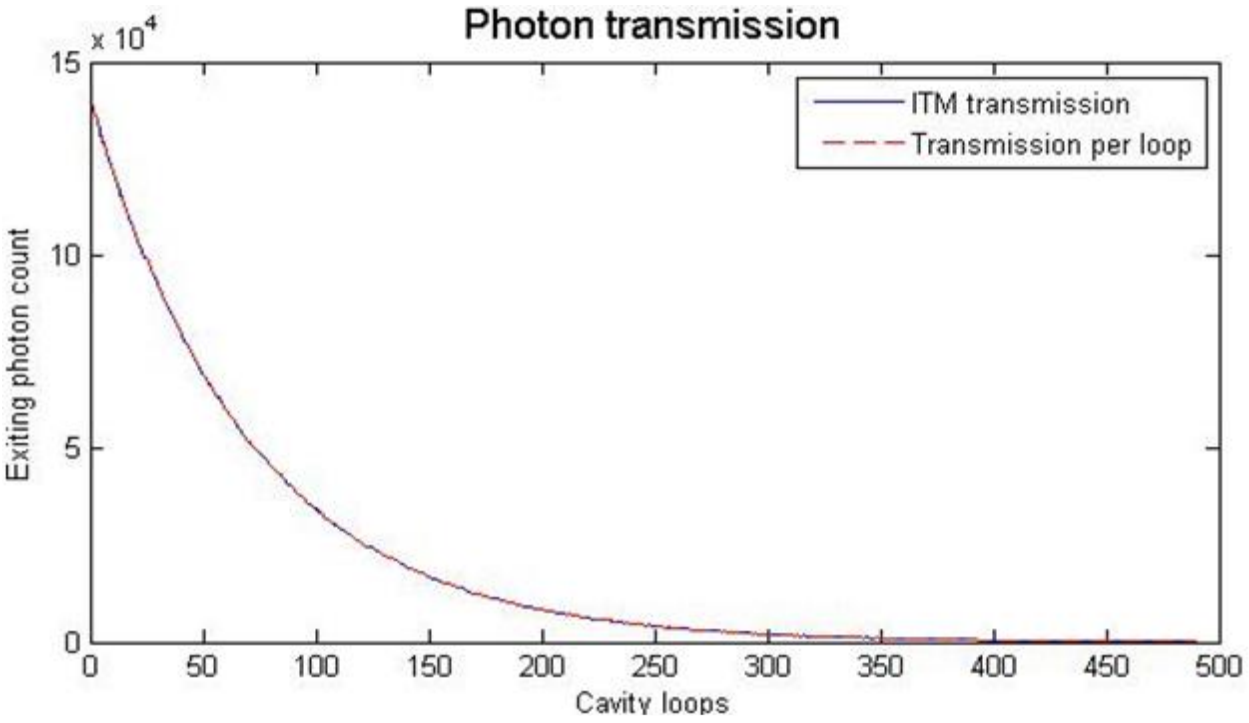


Figure 10 (copy of Appendix C's 2nd plot)

$N = 10{,}000{,}000$ $n_{50\%} = 50$ $n_{1\%} = 327$ $n_{0.1\%} = 490$

This behavior is also confirmed by taking the geometric sum of equation 18

$$I_{out} = I * (1 - R_1R_2) * \frac{1 - (R_1R_2)^n}{(1 - R_1R_2)} \quad (19)$$

which has theoretical limitations $I_{out} = I \Rightarrow n = \infty$

but percentage solutions like $I_{out} = .999 * I \Rightarrow n = 490$

a result that alludes the parallel nature of this application to the first model.

The following figures (11a-c) were generated in a fashion similar to the appendices, but the cavity population is presented as a ratio $\frac{S_n}{I}$ and the exiting intensity plot is given as the ratio $\frac{I_{out}}{I_{in}}$ so as to better display the saturation percentage. In both plots, the 50%, 99%, and 99.9% saturation points are marked for reference and comparison. However, it can be seen in the code implementation that $I_{out}$ shows increased stochastic behavior for larger cavity population. This error ultimately terminated the function prematurely, though this error was reduced with larger values of $I$.

Though this model turns out to be too computationally expensive for my personal computer to run efficiently, this exercise does show some promising features. The first is the cavity population plot does approach an asymptotic saturation around the expected ratio growth of 71.38. Secondly, even though the functions end prematurely, the plots display enough information to show that the 50% saturation point remains at $n = 50$ while the later plots present the 99% saturation residing approximately $n = 327$. To improve my analysis, my next steps would look to apply a curve fit to the “Exit Intensity” plots and see if they would more clearly represent the expected results.

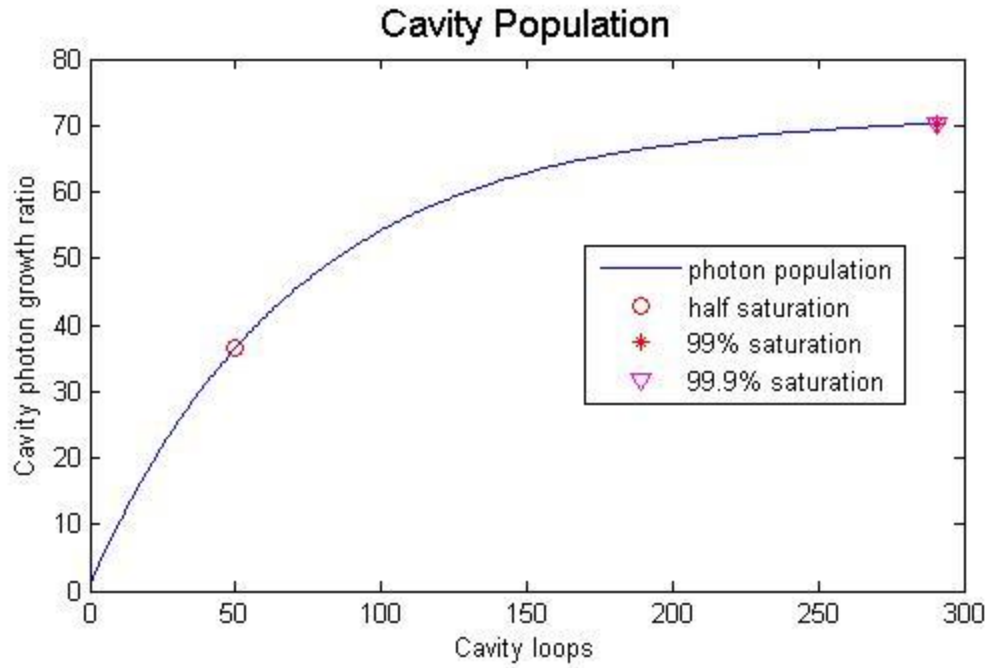


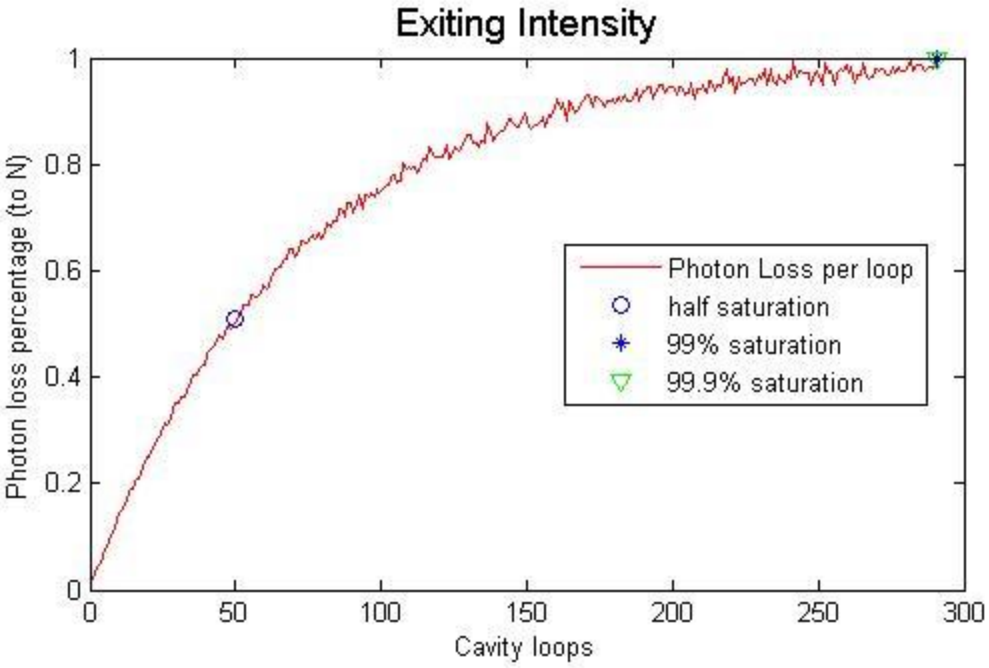


Figure 11a - $I = 10{,}000$ and $n$ cutoff $= 291$

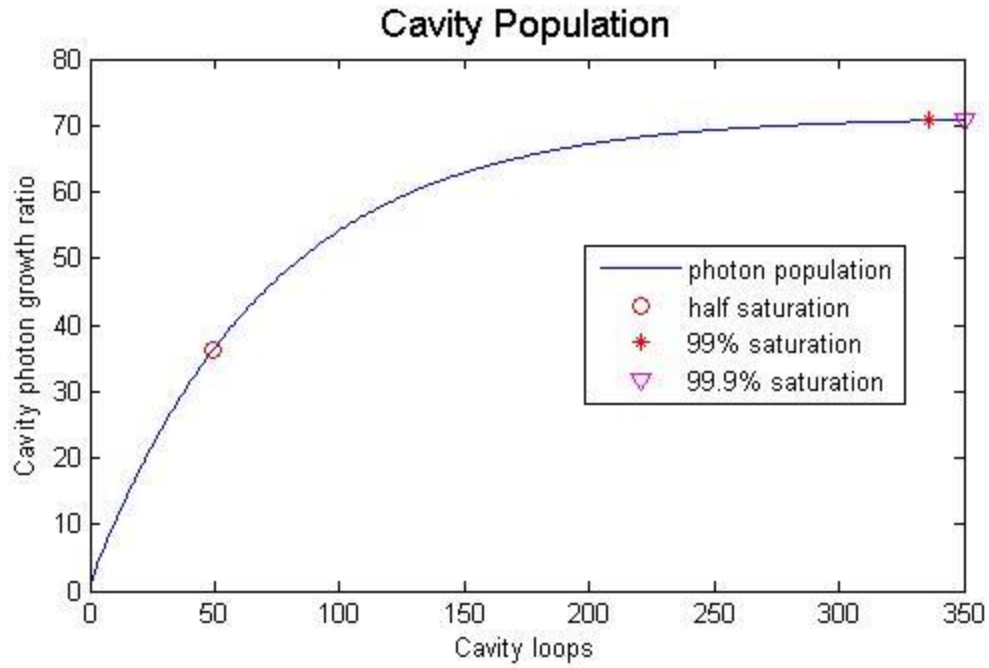


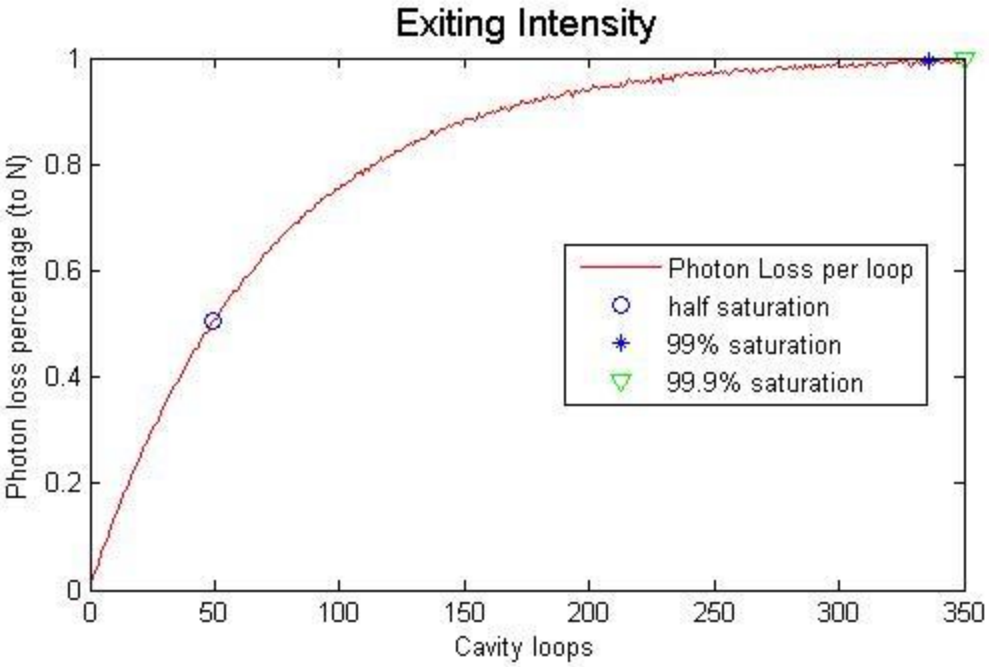


Figure 11b - $I = 100{,}000$ and $n$ cutoff $= 350$

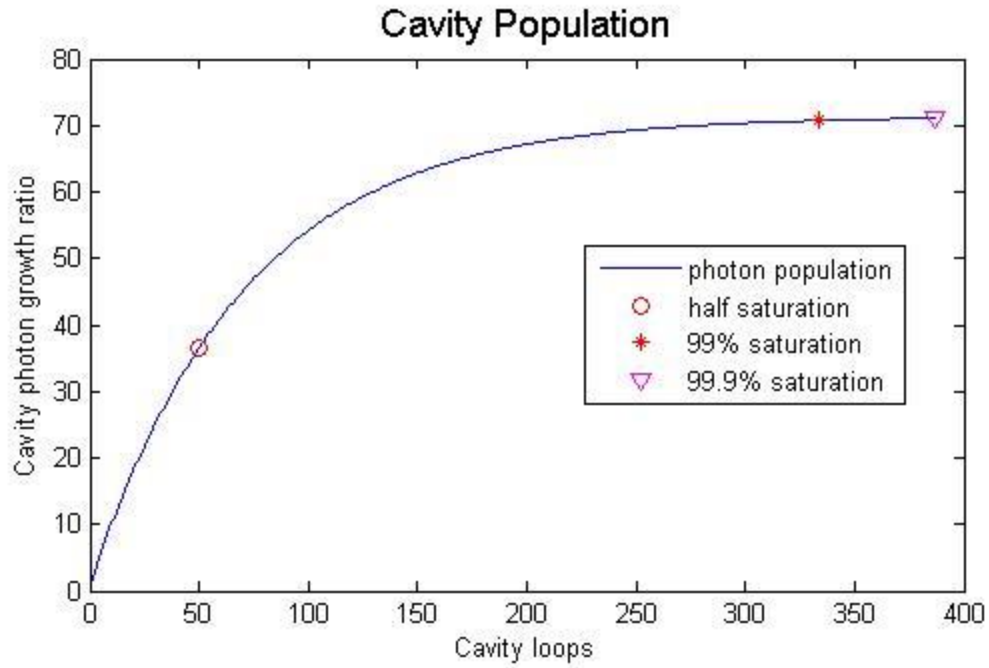


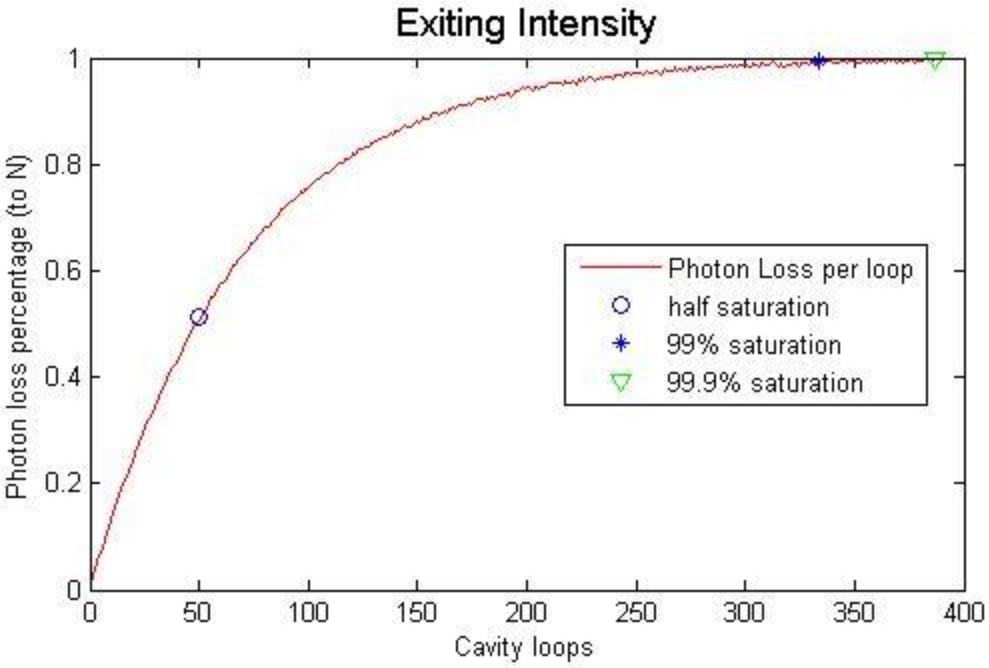


Figure 11c - $I = 200{,}000$ and $n$ cutoff $= 387$

LIGO itself is an exemplary feat in modern engineering and scientific innovation, a solution to a singular theory conceived about one century ago. As gravity itself has been an elusive phenomenon for many centuries, Einstein's theory that gravity travels as a wave at the speed of light was the source needed to instigate its subsequent measurement. When the only two confirmed sources operating at the same rate are light itself and material response to light, optical sciences gained an added focus of development (especially when the latter proved to be unfruitful in gravitational detection attempts). Scientists were guided to the fields of interferometry, Fabry-Perot cavities, laser physics, and material analysis of media and coatings.

What impresses me most about LIGO's development is the foresight of system analysis, the entire chamber to "allow a full confirmation of the design performance" in addition to capable observation (Vogt 36) [7]. In analyzing its own efficiency, LIGO was able to identify a myriad of noise sources, commence research projects to mitigate or correct flaws, and improve itself. It appears that their strategy could be summarized as "let's limit all noise to the extent that gravity itself is the only thing that could alter this device", a thought that puts a grin on my face but paid off in the end. After decades of this process, both facilities in Hanford, Washington and Livingston, Louisiana were able to

collaboratively detect a gravitational event on September 14, 2015 [6]. From that point; engineering, research, and optics continue to move onward; just like gravity.

## Works Cited

[1] "Wave Equation", Wikipedia, 9 Mar 2016. [Online]. Available: https://en.wikipedia.org/wiki/Wave_equation. [Accessed 24 Mar 2016].

[2] Interference and interferometry. (2015) In T. D. Milster (Comp.), *OPTI 505R: Diffraction and Interferometry* (Ch. 4, pp. 1-134). Tucson, Arizona: University of Arizona.

[3] "Michelson Interferometer", Wikipedia, 16 Jan 2016. [Online]. Available: https://en.wikipedia.org/wiki/Michelson_interferometer. [Accessed 24 Mar 2016].

[4] "Fabry-Pérot Interferometer", Wikipedia, 31 Mar 2016. [Online]. Available: https://en.wikipedia.org/wiki/Fabry%E2%80%93P%C3%A9rot_interferometer. [Accessed 11 Mar 2016].

[5] "Fresnel Equations", Wikipedia, 28 Mar 2016. [Online]. Available: https://en.wikipedia.org/wiki/Fresnel_equations#cite_note-Sernelius-3. [Accessed 12 Mar 2016].

[6] Abbot, B. P., et al. "Observation of Gravitational Waves from a Binary Black Hole Merger." *Physical Review Letter* 116 (2016): 061102. Web. 10 Mar 2016. <http://journals.aps.org/prl/pdf/10.1103/PhysRevLett.116.061102>.

[7] Vogt, Rochus E., et al. "A Laser Interferometer Gravitational-Wave Observatory (LIGO)." *California Institute of Technology* 1 (1989): 3-B17. Web. 16 Mar 2016. <https://dcc.ligo.org/public/0065/M890001/003/M890001-03%20edited.pdf>.

[8] "Advanced LIGO Reference Design." *LIGO Laboratory* 2 (2011): 1-49. Web. 16 Mar 2016. <https://dcc.ligo.org/public/0001/M060056/002/AdL-reference-design-v2.pdf>.

[9] "About aLIGO", LIGO Caltech. [Online]. Available: https://www.ligo.caltech.edu/page/about-aligo. [Accessed 10 Mar 2016].

## Works Referenced

"Reflectance", Wikipedia, 6 Feb 2016. [Online]. Available: https://en.wikipedia.org/wiki/Reflectance#cite_note-ILV-4. [Accessed 12 Mar 2016].

"Advanced LIGO – The Next Step in Gravitational Wave Astronomy," Massachusetts Institute of Technology. 20 Nov 2015. [Online]. Available: https://www.advancedligo.mit.edu/. [Accessed 15 Mar 2016].

"Advanced LIGO" *LIGO Scientific Collaboration* 5 (2014): 1-40. Web. 16 Mar 2016. <http://arxiv.org/ftp/arxiv/papers/1411/1411.4547.pdf >

Tables

Table 1

*Reference Design Parameters*

| Subsystem and Parameters | Advanced LIGO Reference Design | Initial LIGO Implementation |
|---|---|---|
| Comparison With initial LIGO Top Level Parameters | | |
| Observatory instrument lengths; LHO = Hanford, LLO = Livingston | LHO: 4km, 4km; LLO: 4km | LHO: 4km, 2km; LLO: 4km |
| Anticipated Minimum Instrument Strain Noise [rms, 100 Hz band] | $< 4x10^{-23}$ | $4x10^{-22}$ |
| Displacement sensitivity at 150 Hz | $\sim 1x10^{-20}$ m/√Hz | $\sim 1x10^{-19}$ m/√Hz |
| Fabry-Perot Arm Length | 4000 m | 4000 m |
| Vacuum Level in Beam Tube, Vacuum Chambers | $<10^{-7}$ torr | $<10^{-7}$ torr |
| Laser Wavelength | 1064 nm | 1064 nm |
| Optical Power at Laser Output | 180 W | 10 W |
| Optical Power at Interferometer Input | 125 W | 6 W |
| Optical power on Test Masses | 800 kW | 15 kW |
| Input Mirror Transmission | 1.4% | 3% |
| End Mirror Transmission | 5-10 ppm | 5-10 ppm |
| Arm Cavity Beam size (1/e^2 intensity radius) | 5.3 cm on ITM<br>6.2 cm on ETM | 4 cm |
| Light Storage Time in Arms | 1.7 ms | 0.84 ms |
| Test Masses | Fused Silica, 40 kg | Fused Silica, 11 kg |
| Mirror Diameter | 34 cm | 25 cm |
| Suspension fibers | Fused Silica Fibers | Steel Wires |
| Seismic/Suspension Isolation System | 3 stage active,<br>4 stage passive | Passive, 5 stage |
| Seismic/Suspension System Horizontal Attenuation | $\geq 10^{-10}$ (10 Hz) | $\geq 10^{-9}$ (100 Hz) |

System parameters used in the mathematical model of LIGO [8].

Table 2

*Mean and Sample Standard Deviation for $n_{50\%}, n_{1\%}$, and $n_{0.1\%}$ for given N ($I = 100k$)*

| ***Mean/SD*** | $\boldsymbol{n_{50\%}}$ | $\boldsymbol{n_{1\%}}$ | $\boldsymbol{n_{0.1\%}}$ |
|---|---|---|---|
| ***N=10*** | *49.8/.4216* | *327.2/2.898* | *490.6/8.249* |
| ***N=20*** | *49.575/.4940* | *326.6/2.415* | *490.25/6.172* |
| ***N=30*** | *49.7/.4661* | *326.4/2.191* | *488/6.314* |
| ***N=40*** | *49.7/.4641* | *327.03/1.954* | *488.93/6.708* |
| ***N=50*** | *49.64/.4849* | *326.54/2.612* | *490.18/7.417* |
| ***N=100*** | *49.76/.4292* | *326.73/2.251* | *490.06/6.380* |
| ***N=125*** | *49.66/.4742* | *327.27/2.208* | *490.08/7.159* |
| ***N=200*** | *49.725/.4476* | *326.77/2.255* | *490.24/7.036* |
| ***N=300*** | *49.737/.4412* | *326.73/2.138* | *489.97/6.499* |

Table 3

*Table of Mean and SSD for N=50 and variable photon count $I$*

| ***Mean/SD*** | $\boldsymbol{n_{50\%}}$ | $\boldsymbol{n_{1\%}}$ | $\boldsymbol{n_{0.1\%}}$ |
|---|---|---|---|
| ***I=100k*** | *49.64/.4849* | *326.54/2.612* | *490.18/7.417* |
| ***I=150k*** | *49.76/.4314* | *326.54/1.693* | *488.84/5.297* |
| ***I=200k*** | *49.8/.4041* | *326.62/1.978* | *489.4/4.990* |
| ***I=250k*** | *49.88/.3283* | *326.6/1.471* | *489.88/3.640* |
| ***I=300k*** | *49.86/.3505* | *327.14/1.161* | *490.22/3.935* |

Appendix A

$N = 100{,}000$ $n_{50\%} = 50$ $n_{1\%} = 326$ $n_{0.1\%} = 497$

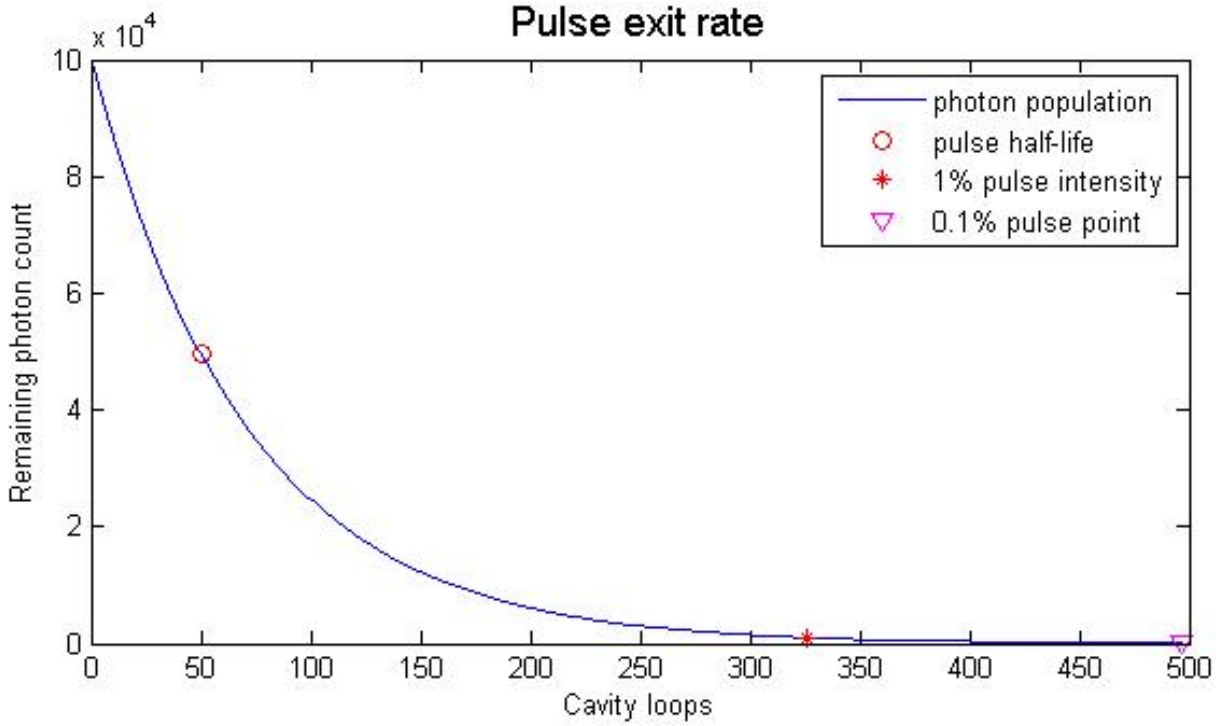


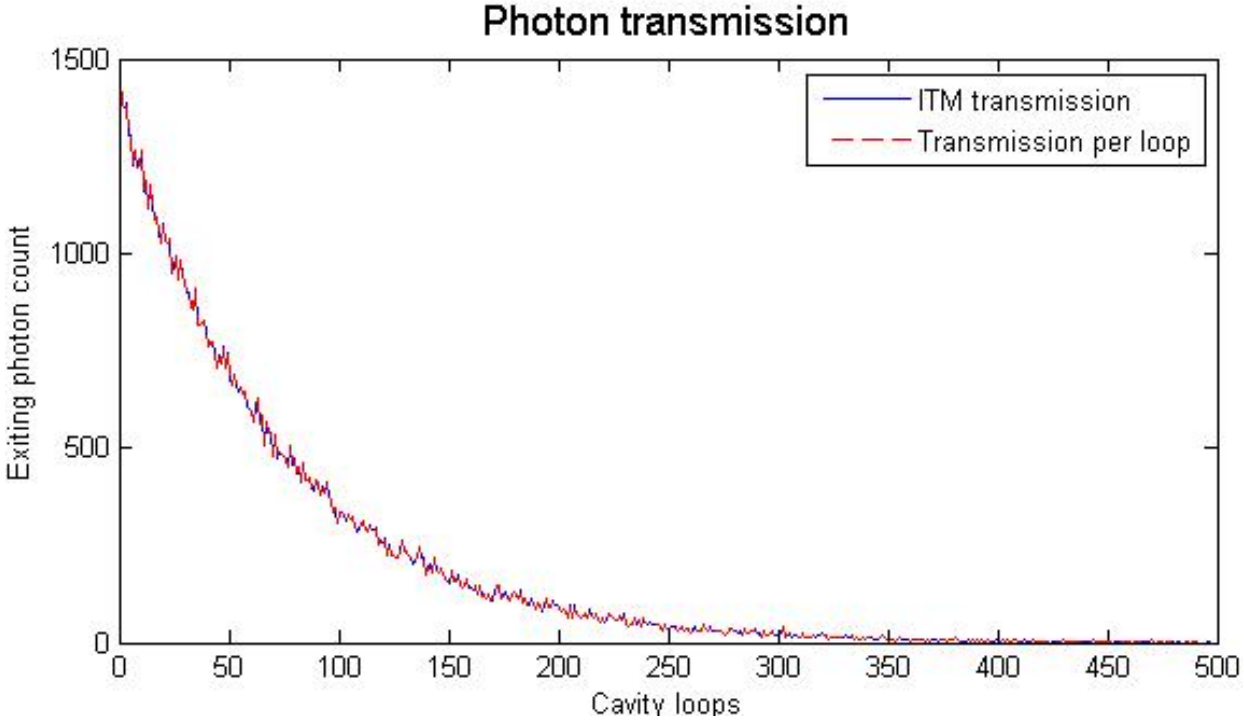

Appendix B

$N = 500{,}000$ $n_{50\%} = 50$ $n_{1\%} = 326$ $n_{0.1\%} = 487$

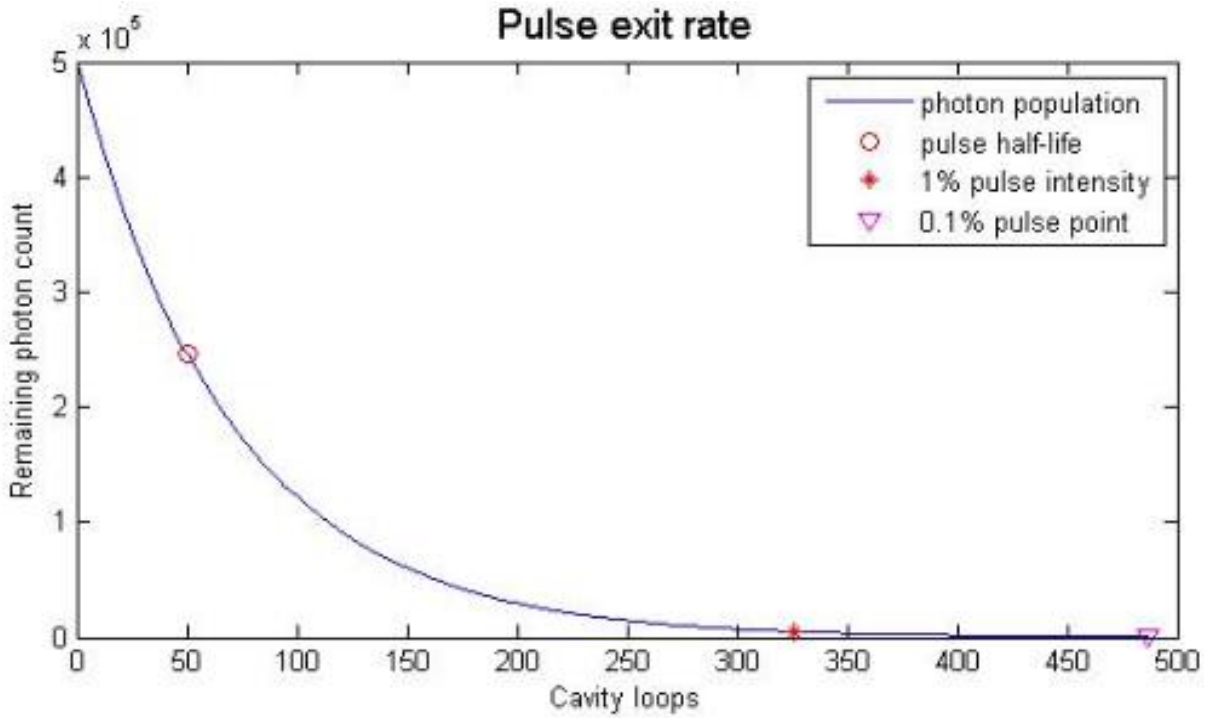


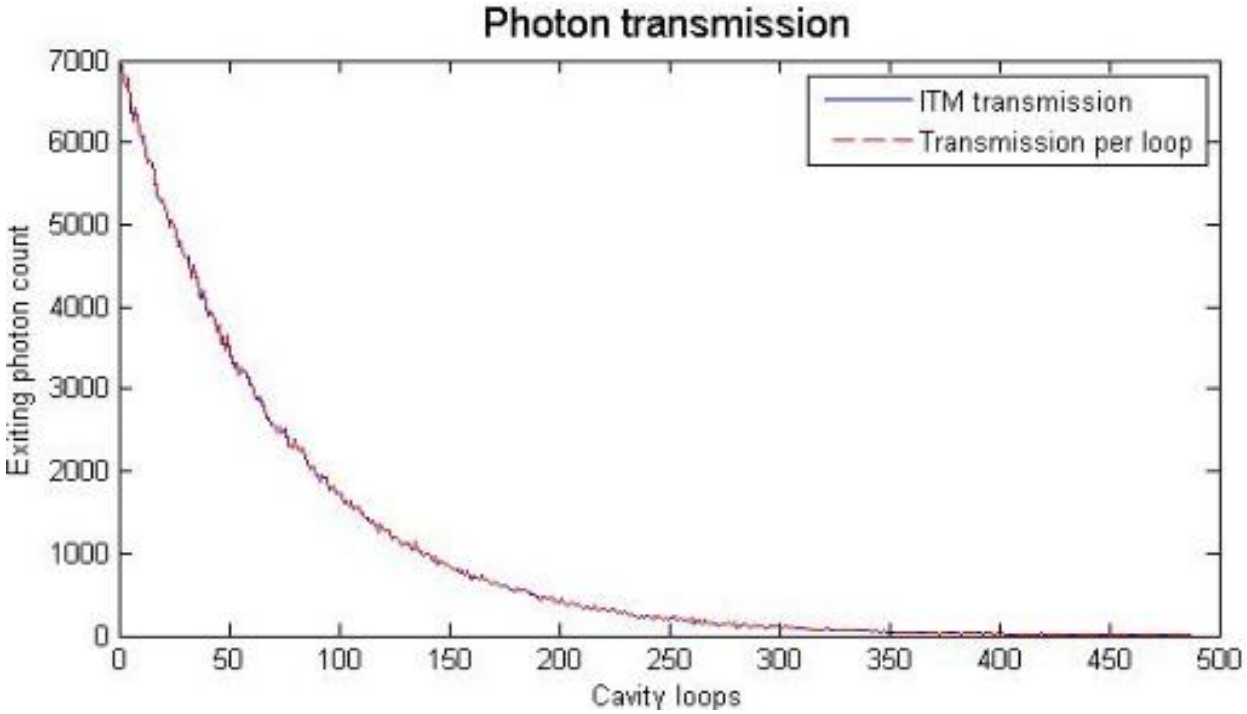

Appendix C

$N = 10{,}000{,}000 \quad n_{50\%} = 50 \qquad n_{1\%} = 327 \qquad n_{0.1\%} = 490$